Morphological Changes of Silica Shells Deposited on Gold Nanorods: Implications for Nanoscale Photocatalysts

Milan Adelt[1], Donald A. MacLaren[2], David J.S. Birch[1] and Yu Chen[1]*

[1] Photophysics Group, Centre for Molecular Nanometrology, Department of Physics, Scottish Universities Physics Alliance, University of Strathclyde, 107 Rottenrow, Glasgow G4 0NG, United Kingdom

[2] SUPA, School of Physics and Astronomy, University of Glasgow, G12 8QQ, Glasgow, United Kingdom

ABSTRACT: Gold nanorods (GNRs) support strong localized surface plasmon resonances that can be exploited to enhance the fluorescence or catalytic properties of adjacent molecules. Coating GNRs with silica is frequently used to functionalize their surfaces, but full encapsulation limits the ability to control the spatial distribution of molecules and their related reactivity. For example, locating molecules near the ends of GNRs would enable their strong longitudinal plasmon resonance to be exploited, but such selectivity is challenging. So far, studies of anisotropic coating have been limited and the mechanism of the adsorption onto GNRs remains unclear. Here, we systematically investigated the anisotropic coating of the ends of GNRs with silica and the influence of growth conditions on the formation of silica shells. Three types of nanostructures have

been observed and their origins are described: fully encapsulated core-shell GNRs, GNRs with only one end coated with silica, and dumbbell-like GNRs (dGNRs) with both ends coated. The study was performed at around room temperature, where the solubility and micellization of the surfactant cetyltrimethylammonium bromide (CTAB) can be tuned to affect the morphology, stability and density of resulting silica shells. Optimized parameters, in combination with an appropriate GNR aspect ratio, are shown to significantly improve the growth yield of dGNRs, which become the dominant product. A protocol for a high yield synthesis of dGNRs was developed, with a maximum yield exceeding 90 %. This study advances our understanding of the growth mechanism of anisotropic coating of GNRs and sheds light on the optimization of site-selective coating processes. The development of anisotropic GNR-based nanostructures for fluorescence/scattering amplifiers will be important in applications such as metal-enhanced fluorescence, surface-enhanced Raman scattering or plasmon-enhanced catalysis.

KEYWORDS: gold nanorods, silica coating, morphology of silica shells, anisotropic coating, formation of silica shells, nanoscale photocatalysts

1. INTRODUCTION

The use of gold nanoparticles in nanoscience has generally depended on their ability to support strong localized surface plasmon resonances (LSPRs)[1–6] and on the ease of modifications of their surfaces.[7–11] The LSPR enhances electromagnetic fields in the vicinity of the metal surfaces,[12] which in turn, can be used to enhance fluorescence, light scattering, photocatalytic process and other properties of nearby molecules.[2,13–18] Gold nanorods (GNRs) in particular have emerged as versatile platforms for these applications due to their tunable optical properties[19–25] as well as their asymmetric shape, which supports the generation of distinct transverse and longitudinal surface

plasmon modes.[26] In order for GNRs to be used as fluorescence/catalytic amplifiers, the molecules to be stimulated should ideally be near the GNR ends, where the strong longitudinal field greatly enhances their molecular or emission properties.[27–30] However, anchoring molecules in this specific area requires site-specific functionalization of the GNR surface.

Silica is one of the most widely used coating agents for noble metal nanoparticles.[31] Due to its optical transparency, porosity and stability,[31–33] a silica shell can be modified with various functional molecules such as photosensitizers and chemotherapeutics[16,17,33] or fluorescent dyes.[34–36] Silica also has a low toxicity, driving a broad range of biomedical applications.[37] Furthermore, a silica layer can be used as a spacer between the GNR surface and adsorbates such as fluorescent dyes, which are otherwise prone to quenching in the proximity of metals. In comparison to the complete encapsulation by silica, coating just the ends of GNRs would facilitate more anisotropic functionalization and more selective excitation of adjacent molecules. Such anisotropic silica coating would be a promising step towards improving the performance of GNRs as fluorescence/catalytic amplifiers but is technically challenging.

GNRs produced via the seed-mediated growth method have their surfaces covered with a positively charged bilayer of the cationic surfactant cetyltrimethylammonium bromide (CTAB).[38,39] CTAB acts as an organic template for the deposition of alkoxysilanes such as tetraethyl orthosilicate (TEOS) to mediate the formation of silica shells.[40] The CTAB bilayer is not uniformly distributed over the surface of GNRs and is assumed to be less densely packed at the GNR ends due to their curvature.[39,41–46] This makes the end-functionalization of GNRs with various coating agents possible.[13,32,41,42,44–49] The resulting anisotropic structures are particularly suitable for photocatalysis, as they allow coating of the ends with, for example, Pd,[46] TiO_2[47] or semiconductors,[50] which can all act as catalysts, while the bare sides of GNRs can directly

participate in oxidation reactions. For example, the LSPR-induced hot electron generation from gold to catalysts enables more efficient electron transfer from the catalyst to molecules of the solvent, which may be used to enhance the hydrogen production under near-infrared illumination.[47,50] Alternatively, Yin et al. demonstrated the use of magnetically active gadolinium-coated dumbbell-like GNRs as tumor-targeted probes for photothermal therapy that are capable of two-photon luminescence as well as being suitable for MRI as contrast agents.[51] The spatial control over the end functionalization also creates additional avenues for surface-enhanced Raman scattering (SERS) or metal-enhanced fluorescence (MEF) which greatly benefit from the strong longitudinal plasmon field of GNRs that can function individually[45] or as dimers[52] that create signal-enhancing hot spots in the gaps between their surfaces.[53]

The deposition of silica on the ends of elongated nanoparticles has previously been achieved through fine control of CTAB and TEOS concentrations.[41,42,44,54] By limiting the concentration of GNRs, thus changing the amount of TEOS available per particle, the morphology of deposited silica shells can be varied between full encapsulation and a dumbbell-like coated GNRs (dGNRs) with a silica sphere attached to each end of the gold core.[42] Additionally, other factors such as the aspect ratio,[55] the width of GNRs or the CTAB chain length[47] have been shown to play important roles in the end-functionalization of GNRs as they all influence the density of the CTAB bilayer on the GNR ends. Moreover, the growth temperature was found to affect the thickness of the mesoporous silica shells,[56] due to the temperature-dependent solubility of CTAB.[56,57] However, to the best of our knowledge, the influence of temperature on the anisotropic coating of GNRs with silica has not been reported. Understanding how temperature and other parameters affect the process of site-selective silica coating of GNRs should provide valuable insight into the mechanism of synthesizing bespoke dGNRs. So far, mechanistic studies have been limited to

investigation of only a few parameters at a time and often do not include quantification of reaction yields of synthesized nanostructures.

In this work, we present a systematic study of the effect of GNR morphology and growth conditions such as temperature and the concentrations of GNRs and CTAB on the morphology of silica shells deposited on GNRs. Three morphologies are examined, from fully encapsulated GNRs (core-shell GNRs) to dumbbell-like, end-coated GNRs (dGNRs) and GNRs with only one end coated with silica (nanolollipops). It was found that variations in morphology are determined by the interplay between all the reaction parameters and the roles of each parameter on the formation of dGNRs are elucidated. We demonstrate a high-yield synthesis of end-functionalized GNRs with silica at a rate exceeding 90 %, to the best of our knowledge the highest yield reported to date.

2. EXPERIMENTAL SECTION

2.1. Materials

Silver nitrate ($AgNO_3$, S6506-5G), gold (III) chloride trihydrate ($HAuCl_4$, G4022-1G), sodium borohydride ($NaBH_4$, 452882-25G), cetyl trimethylammonium bromide (CTAB, H6269-500G), ascorbic acid (A5960-25G), tetraethyl orthosilicate (TEOS, 86578-250ML), sodium hydroxide (NaOH, S5881-500G-M), methanol (≤ 99.8%, 32213-M) and ethanol (≥99.8%) were purchased from Sigma Aldrich. Distilled water was used as a solvent in the synthesis of GNRs.

2.2. Synthesis of gold nanorods

CTAB-coated GNRs were prepared using an adapted standard seed-mediated growth method,[38] consisting of two steps: (1) the preparation of the seed solution; and (2) the subsequent growth of seeds in the growth solution.

10 mL of the seed solution was prepared by mixing 9.75 mL of 0.1M aqueous CTAB solution with 0.25 mL of 0.01M $HAuCl_4 \cdot 3H_2O$. The solution was then stirred for 10 min, then 0.6 mL of

0.01M $NaBH_4$ (prepared in ice-cold water) was added under vigorous stirring for 5 min. After that, the seed solution was left to stand in the dark for 3 hours to allow the growth of the seeds.

10 mL of growth solution was prepared by mixing 9.5 mL of 0.1M aqueous CTAB solution with 0.5 mL of 0.01M $HAuCl_4 \cdot 3H_2O$. The solution was stirred for 10 min before adding 15, 45, 50 or 60 μL of 0.1M $AgNO_3$ to tune the wavelength maxima of the longitudinal plasmon resonance of our GNRs to ~628, 726, 742 or 748 nm (Figure S1).[20] After an additional 5 min of stirring, 55 μL of 0.1M ascorbic acid was added. The final step was the addition of 12 μL of seeds under gentle stirring. The solution was then stored in the dark to age overnight at room temperature. The following day, GNRs were purified via centrifugation (Sigma 1-4 Microfuge) at 12 000 g for 20 min. The supernatant was then extracted, and the pellet re-suspended in distilled water to achieve the desired concentration.

After the purification, extinction spectra of the newly prepared GNR solution were measured using a Lambda 2 UV/VIS spectrometer (PerkinElmer) to determine the maximum wavelength of the longitudinal plasmon band. The concentration of the GNR solution was calculated from the extinction at the longitudinal plasmon band maximum and corresponding molar extinction coefficients at the longitudinal plasmon band maxima (2.6, 3.9 and $4.1 \cdot 10^9$ $M^{-1}.cm^{-1}$ for GNRs with plasmon resonances at 628, 726 and 742, 748 nm). The GNR dimensions and hence aspect ratios (the ratio of length to diameter) and errors (as sample standard deviations) were measured manually for more than one hundred nanoparticles from STEM images using image processing software ImageJ.

2.3. Silica-coated gold nanorods

Silica coating was carried out via the modified single-step silica coating method developed by Gorelikov.[34,40] CTAB-capped GNRs, synthesized in the previous step, were centrifuged for a

second time at 11 200 g for 20 min to remove excess CTAB from the solution and bring the CTAB concentration to approximately <0.01 mM.[34] Further on in the process, a close control of the CTAB concentration is essential, which is achieved after centrifugation by removing the supernatant and re-suspending the pellet in 1.2, 1.4 and 1.6mM aqueous CTAB solutions (3 mL) so that final concentrations of GNRs were ~0.6 nM and ~1 nM. Adding CTAB solutions to pellets ensures more accurate control over the reaction conditions. Suspensions were mixed overnight to allow CTAB to equilibrate on the nanorod surface prior to silica coating. The next day, 12 μL of 0.1M NaOH was added to each 3mL sample to set the pH to approximately 10.5, and the solutions were mixed for 30 min. Then, 27 μL of 20vol% TEOS in methanol was added and mixed for 5 min to homogenize TEOS in the reaction mixture. After 5 min, each sample was transferred to three 1.5 mL centrifuge tubes (1 mL in each tube) and placed in a shaker (ThermoMixer, Eppendorf) for shaking at 19, 21 or 23 °C and at 700 rpm overnight. At lower speed, a certain degree of sedimentation could occur. The GNRs were then centrifuged at 8 000 g for 20 min. Supernatant was removed from each tube and the pellet was re-suspended in 1 mL of a mixture of ethanol and water (3:2), bringing the total volume of each sample to 3 mL. The yields of synthesized nanoparticles were calculated from STEM images as fractions of more than one hundred nanoparticles against their total count in each sample.

It should be noted that all samples compared in each table were synthesized in parallel. Two batches of GNRs of different aspect ratios were used in the two separate studies presented in Table 2 and 3. Moreover, a fresh bottle of TEOS was used for the silica coating of samples in section 3.3 and 3.4. Therefore, relative lower yields of core-shell GNRs and improved yields of end-coated GNRs for GNR2 in Table 3 compared with that in Table 2, despite the higher aspect ratio of GNRs used in the section 3.2, could be attributed to the better reactivity of the fresh TEOS that is prone

to polymerization. Nevertheless, comparison between the same batch of samples and the understanding achieved is valid.

2.4. Characterization

High-angle annular dark-field scanning transmission electron microscopy (HAADF-STEM) and transmission electron microscopy (TEM) data were recorded on a probe-corrected JEOL ARM200cF instrument with a cold field emission source operating at an acceleration voltage of 200 kV. Elemental mapping was performed by electron energy-loss spectroscopy (EELS) using a Gatan 965 Quantum ER post-column spectrometer. Scanning electron microscopy (SEM) images were acquired using a field-emission environmental scanning electron microscope (FEI Quanta 250 FEG-ESEM) with a modular STEM detector at an acceleration voltage of 30 kV. Samples were prepared by drop-casting 5 μL of a sample solution onto a carbon-coated 300-mesh holey Cu grid (Agar Scientific) which was left to dry at room temperature.

3. RESULTS AND DISCUSSION

3.1. Influence of temperature and CTAB concentration on the anisotropic silica coating of GNRs

For the synthesis of end-coated nanoparticles and to identify the effect of individual reaction conditions, CTAB-capped GNRs with an aspect ratio of ~3.3 (42.8 ± 4.3/13.0 ± 1.8 nm) and GNR concentration ([GNR]) of ~1 nM were coated with silica via the modified single-step silica coating method[40] (Figure S1a). We first varied the concentration of CTAB ([CTAB]) to be ~1.2, 1.4, 1.6 mM at selected temperatures: 19, 21, 23 °C (Table 1). To ensure accurate [CTAB] for comparison, GNRs were purified twice via centrifugation to reduce the residual [CTAB] (<0.01 mM) well below working concentrations.[39,48] Purified GNRs were then dispersed in CTAB solutions of defined [CTAB]. Resulting samples were characterized via scanning transmission electron

microscopy (STEM) (Figure 1) that revealed 3 populations of nanostructures – dGNR, core-shell GNR and nanolollipops – with various reaction yields. Table 1 lists the experimental conditions and corresponding yields (%) of the three populations of GNR structures.

The process of end-selective coating of GNRs is based on the same principle as the synthesis of mesoporous silica in the presence of CTAB.[58] First, alkoxysilanes (i.e. TEOS) undergo a base-catalyzed hydrolysis followed by condensation of silica precursors to form silica oligomers. Subsequently, CTAB/silica particles, aggregates of CTAB molecules and oligomers of silica, are formed. The final step is formation of mesopores through aggregation of CTAB/silica particles and further deposition of CTAB molecules and monomers of silica. When silica is being deposited on CTAB-capped gold nanoparticles, the conditions have to be set accurately so that the majority of CTAB molecules are adsorbed on the gold surface, where CTAB serves as a structure directing agent and promotes the aggregation of CTAB/silica particles directly on nanoparticles' surfaces.[40,58] The CTAB bilayer on the ends of GNRs is known to be less compact than that on the sides of GNRs (Figure 1a).[39,41–44] This presents less steric hindrance for the deposition of silica, allowing hydrolyzed TEOS species to access GNR ends and condense.[41,42,44,48] To achieve the delicate non-uniform distribution of the CTAB bilayer, two populations of CTAB must be considered - free CTAB (fCTAB) and CTAB bound to GNRs (bCTAB). High concentration of fCTAB may cause saturation of the GNR surface with a dense CTAB bilayer,[47] which consequently raises the concentration of positively charged CTAB micelles in the solution.[48] As a result, free silica nanoparticles can be generated or GNRs will grow full shells.[48] Thus, bCTAB and components of fCTAB compete in the attraction of negatively charged, hydrolyzed TEOS species.[48] The reaction dynamics of CTAB are dependent on the reaction temperature. The Krafft temperature represents the temperature below which micelles do not form as the maximum

solubility of the surfactant does not reach the critical micelle concentration (CMC,~1 mM[39]).[57] No silica shells form bellow the Krafft temperature. For CTAB in an aqueous solution, this temperature has been reported to be between 20 and 25 °C.[56,57]

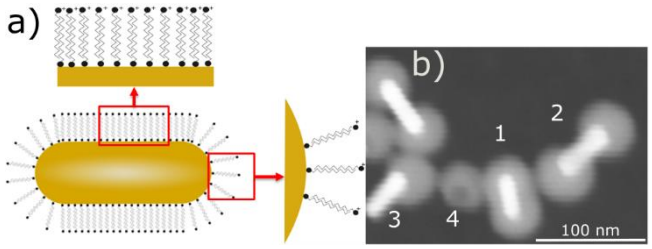

Figure 1. a) Schematic representation of the distribution of CTAB on the surface of GNR and b) a STEM image of a sample containing a representative mixture of (1) core-shell, fully encapsulated GNRs, (2) dGNRs and (3) nanolollipops with a (4) separated silica sphere.

Table 1. Synthesis parameters and % yields of silica-coated GNRs.[a]

Sample	1.2a	1.2b	1.2c	1.4a	1.4b	1.4c	1.6a	1.6b	1.6c
CTAB [mM]	1.2	1.2	1.2	1.4	1.4	1.4	1.6	1.6	1.6
GNR [nM]	1	1	1	1	1	1	1	1	1
T [°C]	19	21	23	19	21	23	19	21	23
Dumbbell [%]	-	*a*	24.5	-	34.1	24.6	-	51.4	27.7
Core-shell [%]	-	*a*	36.0	-	21.2	73.9	-	28.4	71.4
Lollipops [%]	-	*a*	39.5	-	44.7	1.5	-	20.2	0.9

[a] Yields of nanoparticles in sample 1.2b (Figure S2a) were not quantified due to non-uniform coating.

It is apparent that temperature and [CTAB] do indeed influence the morphology of silica shells. The yield of dGNRs and nanolollipops decreased while that of core-shell GNRs increased with

increasing temperature. Silica coating was not observed at 19 °C and was not uniform at low [CTAB] at 21 °C. The absence of coating for all samples at 19 °C can be explained by the low solubility of CTAB, which is likely to remain crystallized below the Krafft point.[56] At 21 °C, sample 1.2b contained non-uniformly coated GNRs and GNRs aggregated mostly in a side-by-side orientation (Figure S2a). This type of aggregation is typical for uncoated GNRs and was likely to be induced by capillary forces during drying.[59,60] The incomplete coating with 1.2 mM of [CTAB] indicates that at 21 °C, CTAB dissolved enough to exceed the CMC, facilitating the formation of CTAB/silica species and their subsequent aggregation on GNRs. However, the amount of CTAB was presumably insufficient to form a uniform coating, which appeared only after a further increase in temperature to 23 °C (sample 1.2c). As [CTAB] was increased to 1.4 and 1.6 mM, the CMC was exceeded even at lower temperature of 21 °C, and more CTAB monomers were available for coating, facilitating the formation of silica shells at 21 °C. At 21 °C and [CTAB] ~1.4 mM, sample 1.4b contained about four times as many end-coated GNRs as core-shell nanoparticles (78.8 %:21.2 %). When [CTAB] was increased to 1.6 mM at the same temperature, the numbers of end-coated GNRs and core-shell GNRs changed only slightly (71.6 %:28.4 %) with a higher ratio of dGNRs in sample 1.6b. The reaction yields of end-coated GNRs changed dramatically at 23 °C compared with results observed at lower temperatures and reached 64 % at [CTAB] ~1.2 mM, while at [CTAB] ~1.4 and 1.6 mM, the ratio reversed and over 70 % of particles were core-shell GNRs. At 23 °C and [CTAB] ~1.6 mM, sample 1.6c also contained a large number of silica nanoparticles (Figure S2b), indicating an abundance of CTAB. Under these conditions, CTAB crystals completely dissolved, which led to an increased concentration of fCTAB, exceeding that of bCTAB, as well as causing the saturation of bCTAB GNR surfaces.

The analysis of STEM images revealed that some GNRs retained only one silica sphere, likely due to the other being torn off by mechanical forces during centrifugation and drying (Figure 2). Several isolated silica spheres in figure 2 show hollow, round-shaped areas which indicate that they originally grew on GNRs. This separation is likely to be due to weak interaction between the silica coating and the GNR, perhaps enhanced by the less compact surfactant bilayer that we exploit for anisotropic coating.

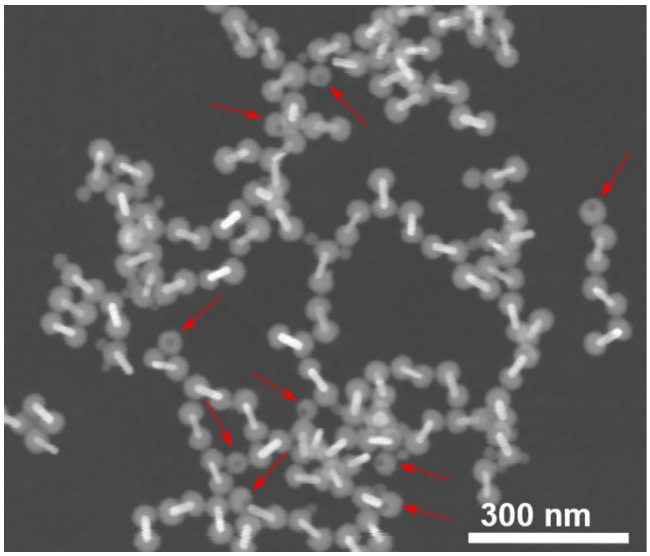

Figure 2. STEM image of end-coated GNRs indicating isolated hollow silica spheres that have been detached from gold cores.

It is noted that at the same [CTAB], the ratio of nanolollipops to dGNRs decreases as temperature increases, suggesting a less porous, thus more robust silica structure, at higher temperature, possibly related to a faster shell assembly rate resulting from the abundance of fCTAB. At low temperatures, when the density of terminal silica spheres is low, we propose that the porous coating is likely to be more fragile at the interface between the gold surface and terminal spheres, making separation from gold cores easier.

Our STEM images have shown dGNRs with separated terminal spheres as well as some dGNRs with overlapping silica that extends from spheres to sides (Figure 3a). Figure 3b shows a TEM image of a dGNR with a thin layer of silica on the side that connects both terminal spheres. The thickness of the side coating can vary from a few nanometers (Figure 3b) to a thicker and more significant overlap (Figure 3a). This side coating could affect further functionalization and result in molecules assembling on both the silica spheres and the silica-coated sides of the GNRs. Side layers could also hinder the oxidation efficiency of bare gold in GNRs when combined with catalysts on their ends. As discussed below, the radius of attached spheres remains approximately 20 nm and is insensitive to growth conditions. This suggests that the growth of dGNRs is self-limiting so that once a maximum end-cap size is achieved growth stops and side layers grow from remaining TEOS and CTAB. This is in agreement with a model that has been used elsewhere to explain the end-functionalization of rod-like NPs and other NPs with tips and edges, in which the functionalization occurs preferentially at curved surfaces due to their unevenly distributed CTAB bilayer, as depicted in figure 3c.[39,41,43,44,47,48] There, the condensation may proceed deeper inside the bilayer than it would be possible on sides where the density of the bilayer is higher (Figure 3d), which allows silica spheres to form (Figure 3S). The thickness of a CTAB bilayer is only 0.8 – 2.2 nm, which is difficult to visualize when GNRs are encapsulated in silica shells with higher density and CTAB chains within the bilayer are compressed or bent.[61,62]

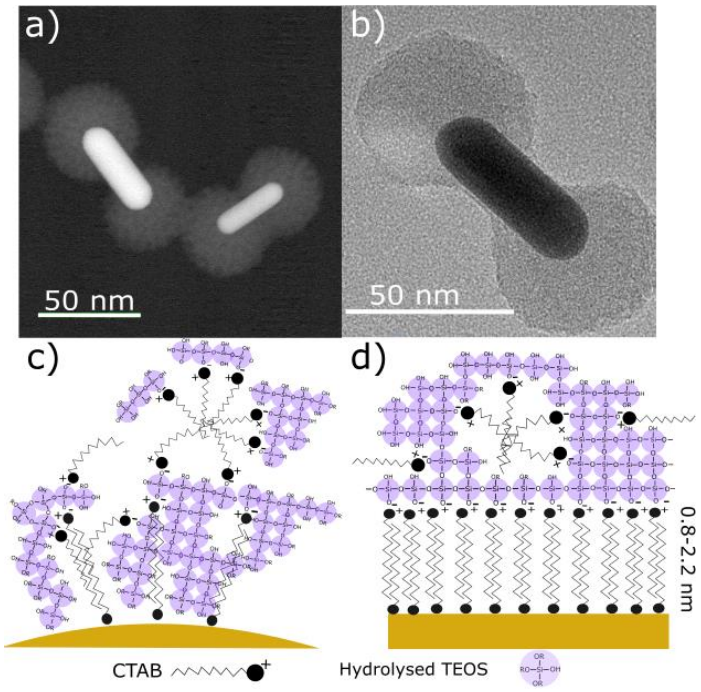

Figure 3. STEM image of dGNRs and porous silica coating a) and TEM image of dGNR with a thin, porous silica layer on the sides of GNRs b). Schematics of the growth of silica (purple) with CTAB chains (black zig zag lines) on ends c) and sides d) of GNRs.

Figure 4 shows elemental mapping of two dGNRs of different aspect ratios, collected using electron energy loss spectroscopy in STEM. Shell material is indicated by the strong presence of Si, O and C, which together are indicative of the incorporation of CTAB and TEOS reaction products inside the silica structure. The top panels are for a relatively long dGNR, for which the growth of the silica spheres has terminated before the spheres overlap. Only a thin silica coating is expected around the middle of the GNR. The bottom panels relate to a shorter GNR, where the silica spheres have grown sufficiently close that the silica coating on the intervening has thickened to produce a 'hybrid' structure that is intermediate between a dGNR and a core-shell GNR. Note that the stronger signal intensities in the lower panels indicate denser silica for the shorter GNR.

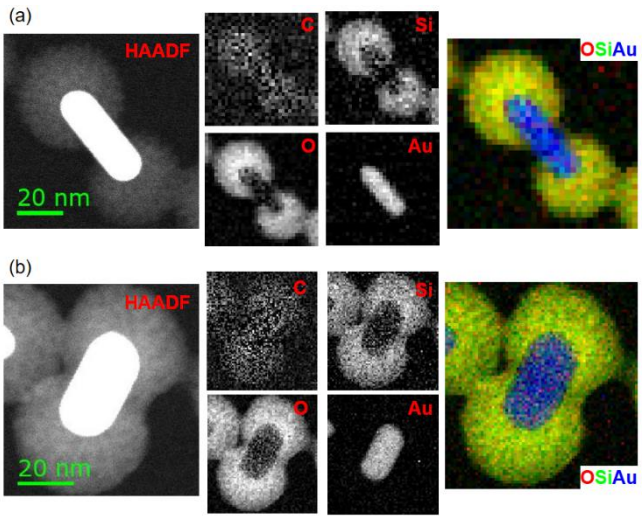

Figure 4. STEM-EELS elemental mapping of two dGNRs with (a) a high and (b) a lower aspect ratio. (Left) A HAADF-STEM image of the spectrum image area, with contrast boosted to reveal the relatively weak signal from the silica shell, which saturates the GNR signal. (Middle) Elemental maps, measured using the K-edges of C, O and Si and the M4,5 edge of Au and following background subtraction. The carbon signal is weak due to the spectrometer acquisition timing. (Right) False-coloured map showing the distribution of (red) oxygen, (green) silicon and (blue) gold, with silica appearing as yellow. The same area is imaged in the HAADF as in the subsequent panels for each GNR, with the scalebar in the HAADF image indicating the GNR size.

CTAB clearly plays a critical role in the synthesis of end-functionalized GNRs by determining the aggregation sites for silica. As will be discussed below, the increased stability of the coating/dumbbell morphology, higher yield of core-shell GNRs and lower yields of nanolollipops observed at higher temperatures all rely on the abundance of CTAB incorporated in shells. The high sensitivity to CTAB and temperature shows the importance of carefully selecting the range of reaction conditions, as even a small deviation in either the reaction temperature or the amount

of CTAB may lead to an irregular coating, generation of core-shell GNRs or unwanted secondary products such as free silica particles.

3.2. The effect of the GNR concentration on the formation of dGNRs

The surface area available for adsorption on precursor GNRs and their aspect ratio are expected to affect the growth mechanism of dGNRs. To investigate the effect of [GNR] on the synthesis of dGNRs, we reduced [GNR] to ~0.6 nM while maintaining other parameters. The [CTAB] was set at ~1.6 mM as the highest yield of dGNRs was produced at this condition. The data were then compared with samples 1.6a-c in Table 2. In contrast to the absence of silica coating observed from previous samples prepared at 19 °C with [GNR] 1nM, sample 1.6d contained over 85 % of end-coated nanostructures. However, the morphology of product nanoparticles shifted to core-shell GNRs when the temperature was increased to 21 and 23 °C. Despite the high yield of end-coated GNRs, it should be noted that synthesis at 19 °C is very sensitive to experimental uncertainty that impairs the reproducibility of the method.

We propose that the decrease of [GNR] at 19 °C resulted in an increased amount of CTAB and TEOS per GNR, which established a bilayer and allowed silica shells to be formed. This also contributed to higher yields of core-shell GNRs formed at temperatures above 21 °C (1.6e,f) compared with [GNRs]~1 nM. This confirms that [GNR] can be used to control the synthesis/yield of the synthesis.[42]

Table 2. Comparison of final growth yields of silica-coated samples with 0.6 and 1nM GNR solutions.

Sample	**1.6a**	**1.6b**	**1.6c**	**1.6d**	**1.6e**	**1.6f**
CTAB [mM]	1.6	1.6	1.6	1.6	1.6	1.6

GNR [nM]	1	1	1	0.6	0.6	0.6
t [°C]	19	21	23	19	21	23
Dumbbell [%]	-	51.4	27.7	40.5	27.4	27.7
Core-shell [%]	-	28.4	71.4	14.5	61.0	65.7
Lollipops [%]	-	20.2	0.9	45.0	11.6	6.6

Because [GNR] ~0.6 nM enabled the production of end-functionalized GNRs at all the investigated temperatures, this concentration was investigated further to determine the effect of aspect ratio on the shell morphology.

3.3. The effect of aspect ratio on the formation of dGNRs

Apart from reagent concentrations, another crucial factor in the silica coating of GNRs that has received little attention is the aspect ratio of gold cores. Wu and co-workers showed that the right combination of the CTAB chain length and diameter of GNRs is important for the end-coating of GNRs with titanium oxide, as both parameters influence the density of the CTAB bilayer.[47] The diameter of GNRs was shown to determine the compactness of the CTAB bilayer by limiting the number of CTAB chains that can cover the gold surface on curved ends. CTAB chains of different lengths exhibit different hydrophobic interactions between molecules as well as different hindrance to approaching coating agents. Terminal curvatures, the width of GNRs and steric hindrance between CTAB chains all change with aspect ratio. Therefore, GNRs with various aspect ratios may yield different numbers of end-coated GNRs and an optimal combination of aspect ratio and [CTAB] is needed to achieve high yield synthesis.

In order to investigate the effect of aspect ratio on the growth of dGNRs, we applied our method of anisotropic silica coating on GNRs with aspect ratios ~2.1 (34.8 ± 6.8/16.5 ± 4.2 nm) (GNR1)

and ~3 (50.6 ± 5.3/16.6 ± 2) (GNR2) (Figure S1b,c). Two temperatures, 21 and 23 °C, were compared. The temperature 19 °C was excluded because of the low surfactant solubility. The amount of TEOS remained unchanged, 27 µL in 3mL solutions. Experimental conditions and corresponding results are summarized in table 3and CTAB are a suitable combination for the synthesis of dGNRs.[47].

Gold nanorods with a low aspect ratio (~2.1) (GNR1_21 – 23) (Figure 5a) formed predominantly core-shell GNRs and notably less dGNRs, whereas the yield of dGNRs containing GNRs with high aspect ratio (~3) (GNR2_21 – 23) increased up to 76.0 % at 23 °C. The significant difference in yields of dGNRs implies a clear dependence of the site-selective coating on aspect ratio. The uniform shape of dGNRs in GNR2_23 (Figure 5b) also suggests that an aspect ratio of ~3 and CTAB are a suitable combination for the synthesis of dGNRs.[47]

Table 3. Summary of experimental conditions used for the anisotropic silica coating of GNRs of various aspect ratios, and the resulting reaction yields of synthesized nanostructures.

Samples	**GNR1_21**	**GNR1_23**	**GNR2_21**	**GNR2_23**
CTAB [mM]	1.6	1.6	1.6	1.6
GNR [nM]	0.6	0.6	0.6	0.6
LSPR [nm]	635	635	726	726
t [°C]	21	23	21	23
Dumbbell [%]	18.8	11.6	48.9	76.0
Core-shell [%]	80.5	86.6	34.4	22.9
Nanololl. [%]	0.7	1.8	16.7	1.0

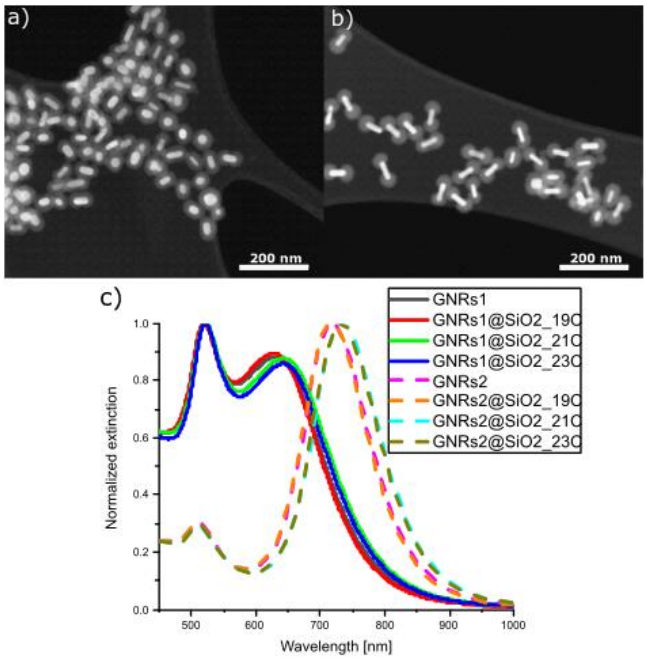

Figure 5. STEM images of a) GNR1_23 and b) GNR2_23 and c) comparison of extinction spectra of gold cores and silica-coated GNRs.

A comparison of extinction spectra (Figure 5c) shows that wavelengths of longitudinal surface plasmon bands of GNRs prepared at 19 °C did not shift with respect to the original GNRs as the coating was not successful at this temperature. At reaction temperatures 21 and 23 °C, extinction spectra were red-shifted by approximately 15 nm upon silica coating compared with uncoated GNRs. The change in the extinction is attributed to the higher refractive index of the silica layer compared with water, which influences the longitudinal plasmon mode due to its sensitivity to changes of refractive index at the surface.[42,44]

Our results suggest that the full coating is the dominant shell morphology on short GNRs. This is probably due to the fact that the length of rods defines the distance between two terminal silica spheres. In the case of short rods, their terminal spheres could be in contact before reaching their self-limiting size. When the two spheres are not energetically favorable anymore, resulting surface diffusion and growth in the neck could lead to a core-shell structure.[4] In contrast, a larger aspect

ratio sets the ends of GNRs farther apart, which facilitates the growth of isolated silica at the endcaps. Silica spheres on long GNRs will remain separate for longer,[55] until the continuous deposition of CTAB/silica particles increases the surface area of silica to the point where attached spheres begin to merge into full shells. This, again, is consistent with the growth model described above.

3.4. Tuning of the optimal growth yield

To further optimize the shape and yields of anisotropically coated GNRs and to reduce the number of core-shell GNRs, the aspect ratio of gold cores was increased to~3.6 (44.3 ± 4.2/12.3 ± 1.9 nm) (Figure S1d) and the amount of TEOS was varied in the range 27, 25, 23 and 21 μL. The reaction temperature was maintained at 23 °C because in the previous step, the highest yields of end-coated GNRs were achieved at this temperature. The decreasing amount of TEOS in combination with the higher aspect ratio of gold cores improved growth yields of dGNRs to >87 %, reaching 91 % when the added volume of TEOS was 23 μL, while yields of core-shell GNRs were reduced to less than 10 % for all three samples (27, 25 and 23 μL) (Figure S4). The above yields of dGNRs are, to the best of our knowledge, the highest values reported in studies of anisotropic silica coating of GNRs.[44,45] When 21 uL of TEOS was added, the total yield of end-coated GNRs was over 90 % but with a relatively large fraction of nanolollipops. As discussed in section 3.1, nanolollipops originated from dGNRs with silica spheres detached from GNRs. It was reported that TEOS at low volumes may not fully surmount the energy barrier of the CTAB bilayer on ends.[45] In these conditions, silica does not reach the gold surface and penetrates the CTAB bilayer only partially. The resulting silica spheres could have lower density foundations and be mechanically less robust, generating more nanolollipops. Even though detached silica spheres were present in all samples, considerably higher yields of dGNRs (>87%) were achieved with most

TEOS volumes used in this study (i.e., 27, 25, 23 μL), indicating an improved efficiency and stability of the dGNR morphology. Furthermore, the thickness of silica coatings was investigated to determine whether varying the amount of TEOS also produces different sizes of end caps. It was found that the radius of attached silica did not vary significantly between the four samples and remained approximately 20 nm. Varying volumes of TEOS in this region to optimize the dGNR yield therefore did not cause significant changes in proportions of terminal silica spheres.

4. CONCLUSIONS

The present study has systemically investigated the effect of various reaction parameters on the morphology of silica coating on GNRs. The key factor in end-functionalization of GNRs was indicated to be the irregular CTAB layer on nanorod ends, which allows the hydrolyzed TEOS species to directly access the gold surface and form silica shells. We observed that temperature significantly influences the shell morphology and the final yield of dGNRs by affecting the solubility of CTAB. The growth of silica is hampered at 19 °C due to the low solubility of CTAB that can be, to some degree, compensated by increasing the concentration of free surfactant in the solution. This hindrance seems to be eliminated at 21 and 23 °C, when sufficient amounts of CTAB are dissolved and are available for the formation of CTAB/silica building blocks that assemble into shells.

Both the temperature and variations in CTAB concentration cause a transition between the three types of nanostructures, yielding more end-functionalized GNRs than core-shell GNRs at lower temperatures and lower CTAB concentrations. The stability of coating improves with increasing temperature and concentration of CTAB, gradually decreasing the number of nanolollipops with separated terminal silica spheres. In some cases, silica can extend to the sides and create a porous layer of varying thickness that links two terminal silica spheres and may represent a potential

complication for further site-selective functionalization. The presence of a silica side layer suggests that silica spheres grow first directly on ends of GNRs and then merge as a result of an ongoing deposition of remaining CTAB with TEOS.

Our results further suggest that the aspect ratio of GNRs determines the stability of the dumbbell shape by establishing the inter-sphere distance as well as the compactness of the CTAB bilayer. Therefore, GNRs with higher aspect ratio seem to be better suited for end-functionalization. The full coating was found to be the dominant shell morphology for GNRs with low aspect ratios. We demonstrate that with the right combination of aspect ratio and reaction parameters, the dumbbell shape as well as the yield of dGNRs may exceed even 90 %, which is the highest yield reported so far.

The dumbbell-like morphology is an interesting platform with two binding sites on its ends that are available for additional surface modification. A direct loading of porous coating with fluorescence or SERS reporters is also possible, so that these nanostructures may find application in metal-enhanced fluorescence and SERS. Fluorophores and other probes that could benefit from the spatially restricted localization and interaction with strong longitudinal plasmon fields are an obvious choice for investigating the enhancing potential of this nanostructure on their performance. Moreover, due to the bare sides of gold cores, gold can directly participate in oxidation reactions when paired with catalysts, which makes them particularly suitable for photocatalytic systems.

ASSOCIATED CONTENT

Supporting Information

STEM images of silica-coated gold nanorods with a non-uniform coating and an abundance of free silica nanoparticles

AUTHOR INFORMATION

Corresponding Authors

Yu Chen – Centre for Molecular Nanometrology, Department of Physics, Scottish Universities Physics Alliance, University of Strathclyde, 107 Rottenrow, Glasgow G4 0NG, United Kingdom

Email: y.chen@strath.ac.uk

Funding Sources

PhD studentship at Strathclyde University by Engineering and Physical Sciences Research Council (EPSRC) (EP/N509760/1)

ACKNOWLEDGMENT

The authors wish to thank Dr. P. R. Edwards for his assistance with the STEM characterisation. M.A. also acknowledges financial support from Engineering and Physical Sciences Research Council (EPSRC) (EP/N509760/1).

REFERENCES

(1) Bauch, M.; Toma, K.; Toma, M.; Zhang, Q.; Dostalek, J. Plasmon-Enhanced Fluorescence Biosensors: A Review. *Plasmonics* **2014**, *9* (4), 781–799. https://doi.org/10.1007/s11468-013-9660-5.

(2) Doria, G.; Conde, J.; Veigas, B.; Giestas, L.; Almeida, C.; Assunção, M.; Rosa, J.; Baptista, P. V. Noble Metal Nanoparticles for Biosensing Applications. *Sensors* **2012**, *12* (2), 1657–1687. https://doi.org/10.3390/s120201657.

(3) Chen, Y.; Preece, J. A.; Palmer, R. E. Processing and Characterization of Gold

Nanoparticles for Use in Plasmon Probe Spectroscopy and Microscopy of Biosystems. *Ann. N. Y. Acad. Sci.* **2008**, *1130*, 201–206. https://doi.org/10.1196/annals.1430.051.

(4) Chen, Y.; Palmer, R. E.; Wilcoxon, J. P. Sintering of Passivated Gold Nanoparticles under the Electron Beam. *Langmuir* **2006**, *22* (6), 2851–2855. https://doi.org/10.1021/la0533157.

(5) Zhang, Y.; Birch, D. J. S.; Chen, Y. Two-Photon Excited Surface Plasmon Enhanced Energy Transfer between DAPI and Gold Nanoparticles: Opportunities in Intra-Cellular Imaging and Sensing. *Appl. Phys. Lett.* **2011**, *99* (10), 103701. https://doi.org/10.1063/1.3633066.

(6) Barnard, A. S.; Chen, Y. Kinetic Modelling of the Shape-Dependent Evolution of Faceted Gold Nanoparticles. *J. Mater. Chem.* **2011**, *21* (33), 12239. https://doi.org/10.1039/c1jm11677k.

(7) Biju, V. Chemical Modifications and Bioconjugate Reactions of Nanomaterials for Sensing, Imaging, Drug Delivery and Therapy. *Chem. Soc. Rev.* **2014**, *43* (3), 744–764. https://doi.org/10.1039/C3CS60273G.

(8) Dykman, L.; Khlebtsov, N. Gold Nanoparticles in Biomedical Applications: Recent Advances and Perspectives. *Chem. Soc. Rev.* **2012**, *41* (6), 2256–2282. https://doi.org/10.1039/C1CS15166E.

(9) Lim, Z.-Z. J.; Li, J.-E. J.; Ng, C.-T.; Yung, L.-Y. L.; Bay, B.-H. Gold Nanoparticles in Cancer Therapy. *Acta Pharmacol. Sin.* **2011**, *32* (8), 983–990. https://doi.org/10.1038/aps.2011.82.

(10) Gu, P.; Birch, D. J. S.; Chen, Y. Dye-Doped Polystyrene-Coated Gold Nanorods: Towards

Wavelength Tuneable SPASER. *Methods Appl. Fluoresc.* **2014**, *2* (2), 024004. https://doi.org/10.1088/2050-6120/2/2/024004.

(11) Wei, G.; Yu, J.; Wang, J.; Gu, P.; Birch, D. J. S.; Chen, Y. Hairpin DNA-Functionalized Gold Nanorods for MRNA Detection in Homogenous Solution. *J. Biomed. Opt.* **2016**, *21* (9), 097001. https://doi.org/10.1117/1.JBO.21.9.097001.

(12) Chen, H.; Shao, L.; Li, Q.; Wang, J. Gold Nanorods and Their Plasmonic Properties. *Chem. Soc. Rev.* **2013**, *42* (7), 2679–2724. https://doi.org/10.1039/C2CS35367A.

(13) Fu, Y.; Zhang, J.; Lakowicz, J. R. Plasmon-Enhanced Fluorescence from Single Fluorophores End-Linked to Gold Nanorods. *J. Am. Chem. Soc.* **2010**, *132* (16), 5540–5541. https://doi.org/10.1021/ja9096237.

(14) Ranjan, R.; Esimbekova, E. N.; Kirillova, M. A.; Kratasyuk, V. A. Metal-Enhanced Luminescence: Current Trend and Future Perspectives- A Review. *Anal. Chim. Acta* **2017**, *971* (April), 1–13. https://doi.org/10.1016/j.aca.2017.03.051.

(15) Lakowicz, J. R. *Principles of Fluorescence Spectroscopy*, 3rd ed.; Lakowicz, J. R., Ed.; Springer US: Boston, MA, 2006. https://doi.org/10.1007/978-0-387-46312-4.

(16) Tham, H. P.; Chen, H.; Tan, Y. H.; Qu, Q.; Sreejith, S.; Zhao, L.; Venkatraman, S. S.; Zhao, Y. Photosensitizer Anchored Gold Nanorods for Targeted Combinational Photothermal and Photodynamic Therapy. *Chem. Commun.* **2016**, *52* (57), 8854–8857. https://doi.org/10.1039/c6cc03076a.

(17) Ke, X.; Wang, D.; Chen, C.; Yang, A.; Han, Y.; Ren, L.; Li, D.; Wang, H. Co-Enhancement of Fluorescence and Singlet Oxygen Generation by Silica-Coated Gold Nanorods Core-

Shell Nanoparticle. *Nanoscale Res. Lett.* **2014**, *9* (1), 666. https://doi.org/10.1186/1556-276X-9-666.

(18) Wei, G.; Simionesie, D.; Sefcik, J.; Sutter, J. U.; Xue, Q.; Yu, J.; Wang, J.; Birch, D. J. S.; Chen, Y. Revealing the Photophysics of Gold-Nanobeacons via Time-Resolved Fluorescence Spectroscopy. *Opt. Lett.* **2015**, *40* (24), 5738. https://doi.org/10.1364/OL.40.005738.

(19) Shao, L.; Woo, K. C.; Chen, H.; Jin, Z.; Wang, J.; Lin, H.-Q. Angle- and Energy-Resolved Plasmon Couplings in Gold Nanorod Dimers. *ACS Nano* **2010**, *3053* (6), 3062.

(20) Zhang, L.; Xia, K.; Lu, Z.; Li, G.; Chen, J.; Deng, Y.; Li, S.; Zhou, F.; He, N. Efficient and Facile Synthesis of Gold Nanorods with Finely Tunable Plasmonic Peaks from Visible to Near-IR Range. *Chem. Mater.* **2014**, *26* (5), 1794–1798. https://doi.org/10.1021/cm403109k.

(21) Murphy, C. J.; Gole, A. M.; Hunyadi, S. E.; Stone, J. W.; Sisco, P. N.; Alkilany, A.; Kinard, B. E.; Hankins, P. Chemical Sensing and Imaging with Metallic Nanorods. *Chem. Commun.* **2008**, No. 5, 544–557. https://doi.org/10.1039/B711069C.

(22) Mbalaha, Z. S.; Edwards, P. R.; Birch, D. J. S.; Chen, Y. Synthesis of Small Gold Nanorods and Their Subsequent Functionalization with Hairpin Single Stranded DNA. *ACS Omega* **2019**, *4* (9), 13740–13746. https://doi.org/10.1021/acsomega.9b01200.

(23) Xu, J.; Gu, P.; Birch, D. J. S.; Chen, Y. Plasmon-Promoted Electrochemical Oxygen Evolution Catalysis from Gold Decorated MnO 2 Nanosheets under Green Light. *Adv. Funct. Mater.* **2018**, *28* (31), 1801573. https://doi.org/10.1002/adfm.201801573.

(24) Zhang, Y.; Wei, G.; Yu, J.; Birch, D. J. S.; Chen, Y. Surface Plasmon Enhanced Energy Transfer between Gold Nanorods and Fluorophores: Application to Endocytosis Study and RNA Detection. *Faraday Discuss.* **2015**, *178*, 383–394. https://doi.org/10.1039/C4FD00199K.

(25) Racknor, C.; Singh, M. R.; Zhang, Y.; Birch, D. J. S.; Chen, Y. Energy Transfer between a Biological Labelling Dye and Gold Nanorods. *Methods Appl. Fluoresc.* **2013**, *2* (1), 015002. https://doi.org/10.1088/2050-6120/2/1/015002.

(26) Jain, P. K.; El-Sayed, M. A. Plasmonic Coupling in Noble Metal Nanostructures. *Chem. Phys. Lett.* **2010**, *487* (4–6), 153–164. https://doi.org/10.1016/j.cplett.2010.01.062.

(27) Khatua, S.; Paulo, P. M. R.; Yuan, H.; Gupta, A.; Zijlstra, P.; Orrit, M. Resonant Plasmonic Enhancement of Single-Molecule Fluorescence by Individual Gold Nanorods. *ACS Nano* **2014**, *8* (5), 4440–4449. https://doi.org/10.1021/nn406434y.

(28) Lakowicz, J. R.; Ray, K.; Chowdhury, M.; Szmacinski, H.; Fu, Y.; Zhang, J.; Nowaczyk, K. Plasmon-Controlled Fluorescence: A New Paradigm in Fluorescence Spectroscopy. *Analyst* **2008**, *133* (10), 1308. https://doi.org/10.1039/b802918k.

(29) Fu, Y.; Zhang, J.; Lakowicz, J. R. Large Enhancement of Single Molecule Fluorescence by Coupling to Hollow Silver Nanoshells. *Chem. Commun.* **2012**, *48* (78), 9726. https://doi.org/10.1039/c2cc34025a.

(30) Ming, T.; Chen, H.; Jiang, R.; Li, Q.; Wang, J. Plasmon-Controlled Fluorescence: Beyond the Intensity Enhancement. *J. Phys. Chem. Lett.* **2012**, *3* (2), 191–202. https://doi.org/10.1021/jz201392k.

(31) Davidson, M.; Ji, Y.; Leong, G. J.; Kovach, N. C.; Trewyn, B. G.; Richards, R. M. Hybrid Mesoporous Silica/Noble-Metal Nanoparticle Materials—Synthesis and Catalytic Applications. *ACS Appl. Nano Mater.* **2018**, *1* (9), 4386–4400. https://doi.org/10.1021/acsanm.8b00967.

(32) Wu, W.; Tracy, J. B. Large-Scale Silica Overcoating of Gold Nanorods with Tunable Shell Thicknesses. *Chem. Mater.* **2015**, *27* (8), 2888–2894. https://doi.org/10.1021/cm504764v.

(33) Fang, L.; Wang, W.; Liu, Y.; Xie, Z.; Chen, L. Janus Nanostructures Formed by Mesoporous Silica Coating Au Nanorods for Near-Infrared Chemo–photothermal Therapy. *J. Mater. Chem. B* **2017**, *5* (44), 8833–8838. https://doi.org/10.1039/C7TB02144E.

(34) Abadeer, N. S.; Brennan, M. R.; Wilson, W. L.; Murphy, C. J. Distance and Plasmon Wavelength Dependent Fluorescence of Molecules Bound to Silica-Coated Gold Nanorods. *ACS Nano* **2014**, *8* (8), 8392–8406. https://doi.org/10.1021/nn502887j.

(35) Ming, T.; Zhao, L.; Yang, Z.; Chen, H.; Sun, L.; Wang, J.; Yan, C. Strong Polarization Dependence of Plasmon-Enhanced Fluorescence on Single Gold Nanorods. *Nano Lett.* **2009**, *9* (11), 3896–3903. https://doi.org/10.1021/nl902095q.

(36) Zhang, Y.; Qian, J.; Wang, D.; Wang, Y.; He, S. Multifunctional Gold Nanorods with Ultrahigh Stability and Tunability for In Vivo Fluorescence Imaging, SERS Detection, and Photodynamic Therapy. *Angew. Chemie Int. Ed.* **2013**, *52* (4), 1148–1151. https://doi.org/10.1002/anie.201207909.

(37) Liberman, A.; Mendez, N.; Trogler, W. C.; Kummel, A. C. Synthesis and Surface Functionalization of Silica Nanoparticles for Nanomedicine. *Surf. Sci. Rep.* **2014**, *69* (2–3),

132–158. https://doi.org/10.1016/j.surfrep.2014.07.001.

(38) Nikoobakht, B.; El-Sayed, M. A. Preparation and Growth Mechanism of Gold Nanorods (NRs) Using Seed-Mediated Growth Method. *Chem. Mater.* **2003**, *15* (10), 1957–1962. https://doi.org/10.1021/cm0207321.

(39) Burrows, N. D.; Lin, W.; Hinman, J. G.; Dennison, J. M.; Vartanian, A. M.; Abadeer, N. S.; Grzincic, E. M.; Jacob, L. M.; Li, J.; Murphy, C. J. Surface Chemistry of Gold Nanorods. *Langmuir* **2016**, *32* (39), 9905–9921. https://doi.org/10.1021/acs.langmuir.6b02706.

(40) Gorelikov, I.; Matsuura, N. Single-Step Coating of Mesoporous Silica on Cetyltrimethyl Ammonium Bromide-Capped Nanoparticles. *Nano Lett.* **2008**, *8* (1), 369–373. https://doi.org/10.1021/nl0727415.

(41) Wang, F.; Cheng, S.; Bao, Z.; Wang, J. Anisotropic Overgrowth of Metal Heterostructures Induced by a Site-Selective Silica Coating. *Angew. Chemie - Int. Ed.* **2013**, *52* (39), 10344–10348. https://doi.org/10.1002/anie.201304364.

(42) Rowe, L. R.; Chapman, B. S.; Tracy, J. B. Understanding and Controlling the Morphology of Silica Shells On. *Chem. Mater.* **2018**, *30*, 6249–6258. https://doi.org/10.1021/acs.chemmater.8b00794.

(43) Hinman, J. G.; Eller, J. R.; Lin, W.; Li, J.; Li, J.; Murphy, C. J. Oxidation State of Capping Agent Affects Spatial Reactivity on Gold Nanorods. *J. Am. Chem. Soc.* **2017**, *139* (29), 9851–9854. https://doi.org/10.1021/jacs.7b06391.

(44) Huang, C.; Chung, M.; Souris, J. S.; Lo, L.-W. Controlled Epitaxial Growth of Mesoporous Silica/Gold Nanorod Nanolollipops and Nanodumb-Bells. *APL Mater.* **2014**, *2* (11),

113312. https://doi.org/10.1063/1.4898415.

(45) Wang, M.; Hoff, A.; Doebler, J. E.; Emory, S. R.; Bao, Y. Dumbbell-Like Silica Coated Gold Nanorods and Their Plasmonic Properties. *Langmuir* **2019**, *35* (51), 16886–16892. https://doi.org/10.1021/acs.langmuir.9b03133.

(46) Ortiz, N.; Hong, S. J.; Fonseca, F.; Liu, Y.; Wang, G. Anisotropic Overgrowth of Palladium on Gold Nanorods in the Presence of Salicylic Acid Family Additives. *J. Phys. Chem. C* **2017**, *121* (3), 1876–1883. https://doi.org/10.1021/acs.jpcc.6b12024.

(47) Wu, B.; Liu, D.; Mubeen, S.; Chuong, T. T.; Moskovits, M.; Stucky, G. D. Anisotropic Growth of TiO2 onto Gold Nanorods for Plasmon-Enhanced Hydrogen Production from Water Reduction. *J. Am. Chem. Soc.* **2016**, *138* (4), 1114–1117. https://doi.org/10.1021/jacs.5b11341.

(48) Zhu, X.; Jia, H.; Zhu, X.; Cheng, S.; Zhuo, X.; Qin, F.; Yang, Z.; Wang, J. Selective Pd Deposition on Au Nanobipyramids and Pd Site-Dependent Plasmonic Photocatalytic Activity. *Adv. Funct. Mater.* **2017**, *27* (22), 1700016. https://doi.org/10.1002/adfm.201700016.

(49) Grzelczak, M.; Pérez-Juste, J.; García de Abajo, F. J.; Liz-Marzán, L. M. Optical Properties of Platinum-Coated Gold Nanorods. *J. Phys. Chem. C* **2007**, *111* (17), 6183–6188. https://doi.org/10.1021/jp0671502.

(50) Wang, H.; Gao, Y.; Liu, J.; Li, X.; Ji, M.; Zhang, E.; Cheng, X.; Xu, M.; Liu, J.; Rong, H.; Chen, W.; Fan, F.; Li, C.; Zhang, J. Efficient Plasmonic Au/CdSe Nanodumbbell for Photoelectrochemical Hydrogen Generation beyond Visible Region. *Adv. Energy Mater.*

2019, *9* (15), 1803889. https://doi.org/10.1002/aenm.201803889.

(51) Yin, J.; Chen, D.; Wu, S.; Li, C.; Liu, L.; Shao, Y. Tumor-Targeted Nanoprobes for Enhanced Multimodal Imaging and Synergistic Photothermal Therapy: Core–shell and Dumbbell Gd-Tailored Gold Nanorods. *Nanoscale* **2017**, *9* (43), 16661–16673. https://doi.org/10.1039/C7NR03847J.

(52) Haidar, I.; Lévi, G.; Mouton, L.; Aubard, J.; Grand, J.; Lau-Truong, S.; Neuville, D. R.; Félidj, N.; Boubekeur-Lecaque, L. Highly Stable Silica-Coated Gold Nanorods Dimers for Solution-Based SERS. *Phys. Chem. Chem. Phys.* **2016**, *18* (47), 32272–32280. https://doi.org/10.1039/C6CP06218K.

(53) Zhang, T.; Gao, N.; Li, S.; Lang, M. J.; Xu, Q. H. Single-Particle Spectroscopic Study on Fluorescence Enhancement by Plasmon Coupled Gold Nanorod Dimers Assembled on DNA Origami. *J. Phys. Chem. Lett.* **2015**, *6* (11), 2043–2049. https://doi.org/10.1021/acs.jpclett.5b00747.

(54) Szychowski, B.; Leng, H.; Pelton, M.; Daniel, M. C. Controlled Etching and Tapering of Au Nanorods Using Cysteamine. *Nanoscale* **2018**, *10* (35), 16830–16838. https://doi.org/10.1039/c8nr05325a.

(55) Li, J. Gold Nanorod Surface Functionalization: Construction of Dynamic Surfaces and Heterogeneous Silica Coating, University of Illinois, 2016.

(56) Baliś, A.; Zapotoczny, S. Tailored Synthesis of Core-Shell Mesoporous Silica Particles—Optimization of Dye Sorption Properties. *Nanomaterials* **2018**, *8* (4), 230. https://doi.org/10.3390/nano8040230.

(57) Manojlovic, J. The Krafft Temperature of Surfactant Solutions. *Therm. Sci.* **2012**, *16* (suppl. 2), 631–640. https://doi.org/10.2298/TSCI120427197M.

(58) Nooney, R. I.; Thirunavukkarasu, D.; Chen, Y.; Josephs, R.; Ostafin, A. E. Self-Assembly of Mesoporous Nanoscale Silica/Gold Composites. *Langmuir* **2003**, *19* (18), 7628–7637. https://doi.org/10.1021/la034522e.

(59) Jain, P. K.; Eustis, S.; El-Sayed, M. A. Plasmon Coupling in Nanorod Assemblies: Optical Absorption, Discrete Dipole Approximation Simulation, and Exciton-Coupling Model. *J. Phys. Chem. B* **2006**, *110* (37), 18243–18253. https://doi.org/10.1021/jp063879z.

(60) Nikoobakht, B.; Wang, Z. L.; El-Sayed, M. A. Self-Assembly of Gold Nanorods. *J. Phys. Chem. B* **2002**, *104* (36), 8635–8640. https://doi.org/10.1021/jp001287p.

(61) Ahmad, I.; Derkink, F.; Boulogne, T.; Bampoulis, P.; Zandvliet, H. J. W.; Khan, H. U.; Jan, R.; Kooij, E. S. Self-Assembly and Wetting Properties of Gold Nanorod–CTAB Molecules on HOPG. *Beilstein J. Nanotechnol.* **2019**, *10*, 696–705. https://doi.org/10.3762/bjnano.10.69.

(62) Venkataraman, N. V.; Vasudevan, S. Hydrocarbon Chain Conformation in an Intercalated Surfactant Monolayer and Bilayer. *J. Chem. Sci.* **2001**, *113* (5–6), 539–558. https://doi.org/10.1007/BF02708789.